The Astrophysical Journal, 980:92 (10pp), 2025 February 10 https://doi.org/10.3847/1538-4357/ad9397

Constraints on Relativistic Jets from the Fast X-Ray Transient 210423 Using Prompt Radio Follow-up Observations

Dina Ibrahimzade[1], R. Margutti[1,2], J. S. Bright[1,3], P. Blanchard[4,5], K. Paterson[6], D. Lin[7], H. Sears[4,5], A. Polzin[8], I. Andreoni[9,10,11], G. Schroeder[4,5], K. D. Alexander[12], E. Berger[13], D. L. Coppejans[14], A. Hajela[15], J. Irwin[16], T. Laskar[17], B. D. Metzger[18,19], J. C. Rastinejad[4,5], and L. Rhodes[3]
[1] Department of Astronomy, University of California, Berkeley, CA 94720-3411, USA; dinaevazade@berkeley.edu
[2] Department of Physics, University of California, 366 Physics North MC 7300, Berkeley, CA 94720, USA
[3] Astrophysics, Department of Physics, University of Oxford, Denys Wilkinson Building, Keble Road, Oxford OX1 3RH, UK
[4] Center for Interdisciplinary Exploration and Research in Astrophysics (CIERA), Northwestern University, Evanston, IL 60202, USA
[5] Department of Physics and Astronomy, Northwestern University, Evanston, IL 60208, USA
[6] Max-Planck-Institut für Astronomie, Königstuhl 17, 69117 Heidelberg, Germany
[7] Department of Physics, Northeastern University, Boston, MA 02115-5000, USA
[8] Department of Astronomy and Astrophysics, The University of Chicago, Chicago, IL 60637, USA
[9] Joint Space-Science Institute, University of Maryland, College Park, MD 20742, USA
[10] Department of Astronomy, University of Maryland, College Park, MD 20742, USA
[11] Astrophysics Science Division, NASA Goddard Space Flight Center, Mail Code 661, Greenbelt, MD 20771, USA
[12] Department of Astronomy/Steward Observatory, 933 North Cherry Avenue, Rm. N204, Tucson, AZ 85721-0065, USA
[13] Center for Astrophysics—Harvard & Smithsonian, 60 Garden Street, Cambridge, MA 02138-1516, USA
[14] Department of Physics, University of Warwick, Gibbet Hill Road, Coventry CV4 7AL, UK
[15] DARK, Niels Bohr Institute, University of Copenhagen, Jagtvej 128, 2200 Copenhagen, Denmark
[16] Department of Physics & Astronomy, University of Alabama, Tuscaloosa, AL 35487-0324, USA
[17] Department of Physics & Astronomy, University of Utah, Salt Lake City, UT 84112, USA
[18] Department of Physics, Columbia University, New York, NY 10027, USA
[19] Center for Computational Astrophysics, Flatiron Institute, 162 5th Avenue, New York, NY 10010, USA
Received 2024 July 10; revised 2024 October 10; accepted 2024 November 7; published 2025 February 5

Abstract

Fast X-ray transients (FXTs) are a new observational class of phenomena with no clear physical origin. This is at least partially a consequence of limited multiwavelength follow-up of this class of transients in real time. Here we present deep optical (*g*- and *i*-band) photometry with Keck, and prompt radio observations with the Very Large Array of FXT 210423 obtained at $\delta t \approx 14$–36 days since the X-ray trigger. We use these multiband observations, combined with publicly available data sets, to constrain the presence and physical properties of on-axis and off-axis relativistic jets such as those that can be launched by neutron star mergers and tidal disruption events, which are among the proposed theoretical scenarios of FXTs. Considering a wide range of possible redshifts $z \leqslant 3.5$, circumstellar medium density $n = 10^{-6}$–10^{-1} cm^{-3}, and isotropic-equivalent jet kinetic energy $E_{k,\rm iso} = 10^{48}$–10^{55} erg, we find that we can rule out wide jets with opening angle $\theta_j = 15°$ viewed within 10° off-axis. For more collimated jets ($\theta_j = 3°$) we can only rule out on-axis ($\theta_{\rm obs} = 0°$) orientations. This study highlights the constraining power of prompt multiwavelength observations of FXTs discovered in real time by current (e.g., Einstein Probe) and future facilities.

Unified Astronomy Thesaurus concepts: X-ray transient sources (1852)

Materials only available in the online version of record: machine-readable table

1. Introduction

Fast X-ray transients (FXTs) are flashes of X-ray emission with timescales between hundreds of seconds to hours and a remarkably large range of intrinsic luminosities spanning several decades (see, e.g., A. Polzin et al. 2023, their Figure 5). Identified in the past decade (A. M. Soderberg et al. 2008; P. G. Jonker et al. 2013; A. Glennie et al. 2015; A. De Luca et al. 2016; J. A. Irwin et al. 2016; F. E. Bauer et al. 2017; G. Novara et al. 2020), FXTs represent an emerging new and heterogeneous observational class of phenomena not well explained by any single model.

Several scenarios have been put forth to explain the physical origin of these events, including both Galactic and extra-galactic origins. Among these is the possibility that FXTs represent the emission originating from the shock break out (SBO) from a core-collapse supernova (CCSN), as a flash of X-ray to UV radiation is expected when the shock wave crosses the surface of the star (e.g., E. Waxman & B. Katz 2017). A possible SBO origin of some FXTs has been suggested by A. M. Soderberg et al. (2008), D. Alp & J. Larsson (2020), G. Novara et al. (2020), and D. Eappachen et al. (2024), although we note that the X-ray transient XRT 080901[20] is the only case with a spectroscopically confirmed optical supernova (i.e., SN 2008D; P. A. Mazzali et al. 2008; A. M. Soderberg et al. 2008; M. Modjaz et al. 2009).

Other proposed interpretations are related to low-luminosity long gamma-ray bursts or short gamma-ray bursts (LGRBs or SGRBs, respectively) viewed off axis (e.g., P. G. Jonker et al. 2013; A. Glennie et al. 2015; F. E. Bauer et al. 2017; N. Sarin et al. 2021; A. J. Levan et al. 2024). The possible connection

[20] The nomenclature "FXT" did not exist at the time of discovery of this transient, hence the "XRT" (or "XRO," i.e., X-ray outburst) name.

with manifestations of SGRB progenitors implies that some FXTs could be produced by a rapidly spinning magnetar remnant that resulted from the merger of two neutron stars (NSs; e.g., H. Sun et al. 2019; Y. Q. Xue et al. 2019; S. Ai & B. Zhang 2021; D. Lin et al. 2022; D. Eappachen et al. 2023, 2024). Mergers between a white dwarf (WD) and an NS represent another interpretation. The properties of the expected transients from these events are not well constrained due to the broad range of physical processes involved (R. Fernández et al. 2019).

Tidal disruption events (TDEs), where the X-rays are emitted as a consequence of the accretion of gas that results from the shredding of a star as it passes too close to a black hole (BH), represent another potential origin. Specifically, given the short timescales of the evolution of FXTs, the tidal disruption of WDs on intermediate-mass BHs (WD-IMBH TDEs; e.g., M. MacLeod et al. 2016; K. Maguire et al. 2020) has been proposed as a possible scenario (e.g., P. G. Jonker et al. 2013; A. Glennie et al. 2015; J. A. Irwin et al. 2016; F. E. Bauer et al. 2017; Z.-K. Peng et al. 2019). Directly relevant to our study, gamma-ray bursts and TDEs can launch relativistic jets (J. S. Bloom et al. 2011; D. N. Burrows et al. 2011; A. J. Levan et al. 2011; B. A. Zauderer et al. 2011; S. B. Cenko et al. 2012; G. C. Brown et al. 2015; D. R. Pasham et al. 2015; Q. Yuan et al. 2016; I. Andreoni et al. 2022a, 2022b; L. Rhodes et al. 2023; J. J. Somalwar et al. 2023).

Other scenarios include emission from X-ray binaries, and Galactic phenomena such as late-type stellar flares (e.g., A. Glennie et al. 2015; A. De Luca et al. 2020) as it was suggested for some XMM-Newton FXTs (D. Alp & J. Larsson 2020). Finally, magnetar outbursts and even exotic scenarios involving the collisions of minor bodies (such as asteroids) with NSs have been considered (e.g., P. G. Jonker et al. 2013). Understanding the origins and progenitors of FXTs is paramount and may also have implications for current gravitational wave (GW) searches (i.e., if indeed associated with binary NS mergers, FXTs could constitute electromagnetic counterparts of GW sources).

While approximately 40 FXTs have been documented up to the end of 2023 (see, e.g., J. Quirola-Vásquez et al. 2022, 2023; D. Eappachen et al. 2024 for recent population studies, and references therein), the vast majority have been discovered through archival data searches (mostly using Chandra or XMM-Newton data) and therefore lack prompt multiwavelength follow up, making their characterization and determination of their physical origin challenging. With the recent launch of the Einstein Probe (EP) in early 2024 (W. Yuan et al. 2022), the detection of FXTs in real time has now become routine. This opens up the possibility of prompt follow up, which is likely to shed new light on the origins of these events.

A notable example in this regard is the recently discovered EP 240315 in the 0.5–4 keV band by W. J. Zhang et al. (2024). Follow up of the event led to the first detection of both an optical and radio counterpart to an FXT and a redshift measurement of $z = 4.859$ (G. Bruni et al. 2024; F. Carotenuto et al. 2024; J. Gillanders et al. 2024; J. K. Leung et al. 2024; A. Saccardi et al. 2024; S. Srivastav et al. 2024). The observed properties of EP 240315 are consistent with an interpretation as an LGRB and illustrate the possibility that a large fraction of FXTs with lower X-ray luminosities may be interpreted as low-luminosity LGRBs (J. Gillanders et al. 2024; A. J. Levan et al. 2024; Y. Liu et al. 2024). J. Gillanders et al. (2024) also recognize that with the current observations, a jetted TDE interpretation cannot be ruled out.

The EP detection of similar events at cosmological distances and in the local Universe will likely continue to shed insight on this potential categorization.

In this paper, we focus on FXT 210423, which was discovered in real time by D. Lin et al. (2021) in Chandra data. Largely based on the observed properties of the X-ray signal, S. Ai & B. Zhang (2021) and D. Lin et al. (2021) propose that FXT 210423 is the manifestation of a rapidly spinning magnetar remnant resulting from a merger of two NSs, like SGRBs. D. Eappachen et al. (2023) present a detailed analysis of the X-ray light curve and spectrum of FXT 210423 along with deep optical imaging of the event, and identify three potential host galaxies. While acknowledging multiple possible origins of the event including a WD-IMBH TDE, SBO, WD-NS merger, or NS-NS merger (including the possibility of a remnant magnetar), D. Eappachen et al. (2023) favor a NS merger scenario. In this work we present deep optical and radio follow-up observations of FXT 210423. We use these observations in combination with simulations to place constraints on the parameter space of relativistic jets in effort to narrow down the the possible origins of the transient and provide future recommendation for prompt multiwavelength follow-up of FXTs.

This paper is organized as follows: In Section 2 we discuss the extraction of the X-ray, radio, and optical data used for our analysis, and we discuss the possible host galaxy association of the event using deep optical imaging. In Section 3 we derive constraints on the presence of relativistic jets like those launched by SGRBs, LGRBs, or TDEs using a large sample of jet simulations. We discuss our findings in Section 4, and we comment on the implications of these results for future follow-up campaigns of FXTs discovered in real time, for example with the EP. We adopt the following cosmology: $H_0 = 69.6\ \mathrm{km\ s^{-1}\ Mpc^{-1}}$, $\Omega_M = 0.286$, and $\Omega_\Lambda = 0.714$.

2. Observations and Data Analysis

2.1. Chandra X-Ray Observations

FXT 210423 was detected on 2021 April 23 (MJD 59327) at 22:22:35.817 UTC until 2021 April 24 at 02:15:05.817 UTC, during a Chandra X-ray Observatory (CXO) calibration observation of A1795 (ObsID:24604) (D. Lin et al. 2021). The source is located on CCD ID3 of the ACIS-I instrument. We reprocessed and reduced the data using the `CIAO` v4.15.1 software package (A. Fruscione et al. 2006) and standard filtering criteria with the goal of obtaining the X-ray flux light curve of FXT 210423. While the CXO data analysis has already been presented in D. Eappachen et al. (2023), a table of corresponding time and flux values of the light curve has not previously been published.

We used the `CIAO` tool `wavdetect` and we detected an X-ray source with significance $\sigma = 10.89$ at sky coordinates R.A. $= 13^{\mathrm{h}}48^{\mathrm{m}}56\overset{\mathrm{s}}{.}46 \pm 0\overset{\mathrm{s}}{.}04$, decl. $\delta = 26°39'45\overset{''}{.}13 \pm 0\overset{''}{.}54$ consistent with those reported in D. Eappachen et al. (2023). Consistent with previous findings, the X-ray emission from FXT 210423 is detected by the CXO for a total of 13.95 ks. Based on the output from `wavdetect`, we used a source extraction region centered at the coordinates above and with radius of $7\overset{''}{.}5$, while we estimated the background contribution using a $60''$ radius circular source-free region. We note that the off-axis source location in the telescope field of view causes a

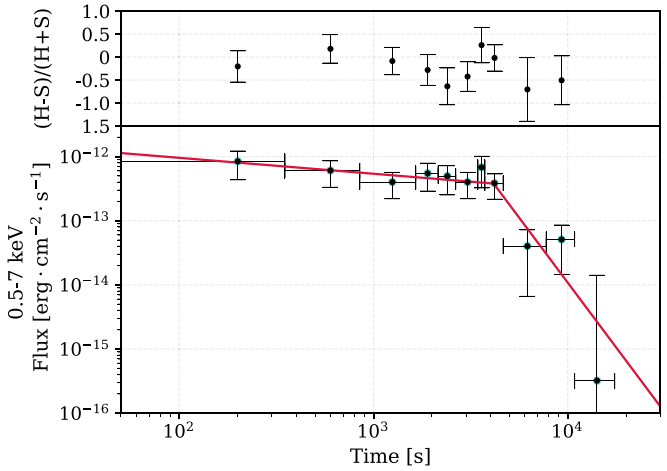

Figure 1. Unabsorbed 0.5–7 keV flux (main panel) and hardness ratio (upper panel) evolution of FXT 210423. The soft band (S) is defined between 0.5 and 2 keV, and the hard band (H) between 2 and 7 keV. No spectral evolution is apparent. The X-ray light curve can be fit with a broken power law (red solid line) with $F_X \propto t^{-0.2\pm0.2}$ at $\delta t < 4.1$ ks steepening to $F_X \propto t^{-4.1\pm1.4}$ at later times.

Table 1
Chandra Unabsorbed 0.5–7 keV Flux Light Curve of FXT 210423 with $F_X \propto t^{-0.2\pm0.2}$ at $\delta t < 4.1$ ks Steepening to $F_X \propto t^{-4.1\pm1.4}$

MJD (day)	Time Since T_0 (s)	Bin Size (s)	Flux (erg cm^{-2} s^{-1})
59327.9324	200	400	$8.44^{+3.77}_{-4.08} \times 10^{-13}$
59327.9370	600	400	$6.08^{+2.53}_{-2.76} \times 10^{-13}$
59327.9445	1250	900	$4.01^{+1.66}_{-1.80} \times 10^{-13}$
59327.9520	1900	400	$5.49^{+2.39}_{-2.59} \times 10^{-13}$
59327.9578	2400	600	$4.97^{+2.25}_{-2.44} \times 10^{-13}$
59327.9653	3050	700	$4.01^{+1.66}_{-1.80} \times 10^{-13}$
59327.9717	3600	400	$6.80^{+3.29}_{-3.54} \times 10^{-13}$
59327.9787	4200	800	$3.85^{+1.54}_{-1.68} \times 10^{-13}$
59328.0018	6200	3200	$4.02^{+3.21}_{-3.36} \times 10^{-14}$
59328.0377	9300	3000	$5.10^{+3.46}_{-3.65} \times 10^{-14}$
59328.0938	14,150	6700	$3.22^{+1.38}_{-1.38} \times 10^{-16}$

Note. Light curve shown in Figure 1.

significantly larger than average point-spread function. The source region contains a total of 140 events in the energy range 0.5–7 keV, corresponding to 108.2 background-subtracted events. We extracted the net count-rate light curves of the source in the energy ranges 0.5–2 keV (soft band) and 2–7 keV (hard band) with `dmextract`. As we show in Figure 1, upper panel, we find no statistical evidence for evolution of the hardness ratio with time, consistent with D. Eappachen et al. (2023). Given the lack of evidence for spectral evolution of the source and the limited photon statistics, we proceeded with the extraction of a single spectrum with `specextract`. We modeled the spectrum as an absorbed power-law model (i.e., `tbabs*ztbabs*pow` within `Xspec`). We set the Galactic neutral hydrogen column density in the direction of the source to $N_{\rm H,MW} = 1.01 \times 10^{20}\,{\rm cm}^{-2}$ (HI4PI Collaboration et al. 2016). We found no evidence for intrinsic absorption, and we thus assumed $N_{\rm H,int} = 0\,{\rm cm}^{-2}$. For this paper we explore a range of potential source redshifts $z = 0.063$, 1.0, 1.5, and 3.5 (Section 3), but we note that the best-fitting X-ray spectral

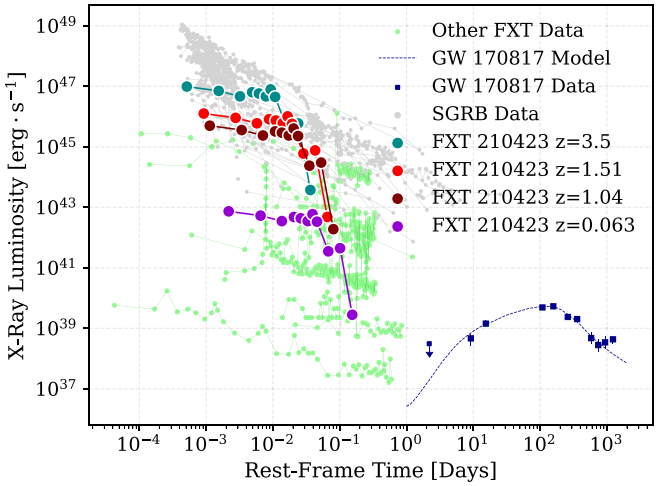

Figure 2. Comparison of the 0.3–10 keV (observer frame) X-ray luminosity vs. rest frame time of FXT 210423 assuming different redshift values, with the X-ray emission from the NS merger event GW170817 from A. Hajela et al. (2022), a collection of SGRB X-ray afterglows from A. Rouco Escorial et al. (2023), and a collection of FXT X-ray light curves from A. Polzin et al. (2023). The X-ray luminosity of FXT 210423 at $z \geqslant 1$ (Section 3) is consistent with that of SGRB afterglows and the more luminous FXTs.

parameters do not significantly depend on z. We employed Cash-statistics for our fits. The best-fitting power-law photon index is $\Gamma = 1.90^{+0.28}_{-0.27}$, where $\Gamma = \beta + 1$ and the specific flux is $F_\nu \propto \nu^{-\beta}$. We used this model to flux calibrate the 0.5–7 keV net count-rate light curve in the 0.5–7 keV energy band. We provide the unabsorbed 0.5–7 keV flux light curve of FXT 210423 in Table 1 and we show the X-ray flux evolution of FXT 210423 in Figure 1. We show the comparison of the X-ray luminosity at four assumed redshift values for FXT 210423 with a collection of FXT X-ray light curves, a collection of SGRB X-ray afterglows, and the X-ray emission from the NS merger event GW170817 in Figure 2. The results from our X-ray analysis are consistent with those from D. Eappachen et al. (2023).

2.2. Radio Observations

We initiated Karl G. Jansky Very Large Array (VLA) radio observations of FXT 210423 under the Director's Discretionary Time (DDT) program VLA/21A-422 (PI: J. Bright) beginning on 2021 May 8. Observations were taken with the VLA in its most compact (D) configuration, and at C-, X-, and Ku-bands using the WIDAR (T. E. Clarke et al. 2016) backend for optimal continuum sensitivity. Data were calibrated using the Common Astronomy Software Applications (CASA; J. P. McMullin et al. 2007) version 6.4.1.12 pipeline version 2022.2.0.64, with 3C286 used to calibrate the bandpass response of the VLA and the absolute flux scale, while J1407 +2827 was used to calibrate the time-dependent gains at all frequencies. The pipeline output was then imaged manually using the CASA task TCLEAN with a briggs robust parameter of 0.5 (D. S. Briggs 1995). Upon imaging the calibrated data, we identified significant residual artefacts around a bright field source, which corrupted the image location around the position of FXT 210423, which persisted after deconvolution. To improve the quality of our images, we performed iterative self-calibration in both amplitude and phase, which allowed us to recover significantly improved images. We do not detect radio emission from XRT210423 in any of our VLA epochs,

Table 2
VLA Observations of FXT 210423

MJD (day)	Time Since T_0 (day)	Frequency (GHz)	Flux Density (μJy beam^{-1})
59342.0883	14.16	10	<27
59342.1118	14.18	6	<26
59346.3537	18.42	15	<16
59349.0692	21.14	10	<48
59349.0928	21.16	6	<26
59350.2819	22.35	15	<14
59363.2973	35.37	15	<15
59364.0282	36.10	10	<27
59364.0519	36.12	6	<35

Note. Upper limits are 3σ and are measured from a representative region around the source location.

but derive constraining upper limits, which are summarized in Table 2. The corresponding radio luminosity from these observations at four assumed redshift values is shown in Figure 3 along with prompt radio observations from additional FXTs and SGRB radio afterglow data for comparison.

In addition to our VLA observations, we include the flux density limits as derived from an observation carried in band-4 (i.e., frequency range 0.55–0.75 GHz) of the Giant Metrewave Radio Telescope (uGMRT) on 2021 June 3 ($\delta t \approx 41$ days under program number DDTC180 (PI: M. Surnis), as reported by M. Surnis et al. (2021). No continuum emission was detected in the direction of FXT 210423, and the observation yielded a 3σ flux density upper limit of 750 μJy at $\nu = 0.65$ GHz (M. Surnis et al. 2021).

2.3. Optical Observations

We obtained imaging of FXT 210423 in the g and i filters with the Low Resolution Imaging Spectrograph (LRIS) mounted on the Keck I Telescope on 2021 May 11, which corresponds to $\delta t \approx 18.03$ days (PI: K. Paterson, program # O316). A dithered sequence of 14 frames, each bias- and flat-field-corrected, were aligned and combined into final deep stacks with total exposure times of 2800 and 2240 s in the g and i bands, respectively. A faint source is detected in both filters at a location consistent with the X-ray position of FXT 210423. The coordinates of the source in the g band are R.A. $= 13^{\rm h}48^{\rm m}56\overset{\rm s}{.}46$, $\delta = 26°39'44\overset{''}{.}76$ with a $0\overset{''}{.}3$ positional uncertainty, which corresponds to a $0\overset{''}{.}36 \pm 0\overset{''}{.}62$ offset from the X-ray position of FXT 210423 and a $0\overset{''}{.}72$ angular offset from the position of the possible host galaxy proposed by D. Eappachen et al. (2023) referred to as "cX" hereafter (see Figure 4). We are unable to calculate the uncertainty on the offset from the X-ray position of FXT 210423 to cX due to limited available details on the position of cX. For "cX," D. Eappachen et al. (2023) infers $m_g = 25.9 \pm 0.1$ mag at $\delta t \approx 48$ days. We measured the flux of the source in our Keck images using aperture photometry calibrated using Sloan Digital Sky Survey (SDSS) catalog stars, finding AB magnitudes of $m_g = 25.80 \pm 0.17$ mag (consistent with the measurements by D. Eappachen et al. 2023) and $m_i = 25.40 \pm 0.25$ mag. Due to the lack of variability in brightness and position, we thus identify our extended g-band source with "cX." The source is slightly extended in the g band making it likely that some of the flux may be due to an underlying faint host galaxy (with unknown redshift). In the following, we thus

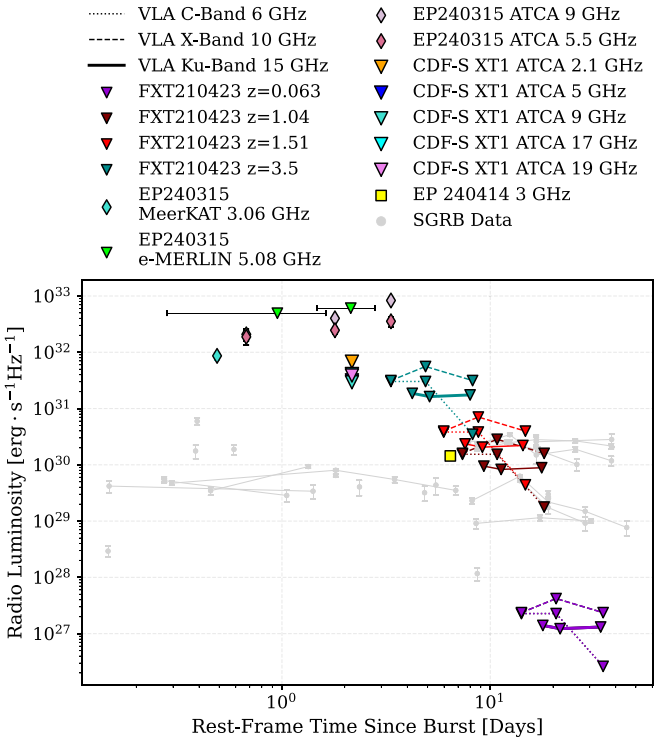

Figure 3. Radio observations of FXT 210423 for four assumed redshift values in the context of radio afterglows of SGRBs at rest-frame frequency 6–15 GHz and other FXTs with prompt radio observations. Triangles represent 3σ upper limits while all other markers represent detections. Radio observations of SGRBs from E. Berger et al. (2005), A. M. Soderberg et al. (2006), W.-f. Fong et al. (2013, 2015, 2022), A. Volnova et al. (2017), F. Knust et al. (2017), W. Fong et al. (2021), A. E. Nugent et al. (2022), and T. Laskar et al. (2022). EP240315 data from J. Gillanders et al. (2024). EP240414 data from P. Jonker (2023) and J. Bright et al. (2024). CDF-S FXT1 data from F. E. Bauer et al. (2017). SRGt J123822.3-253206, a source consistent with the features of an FXT with radio counterpart (A. Y. Q. Ho 2020; A. Semena et al. 2020; J. Wilms et al. 2020) is not shown in this plot due to the lack of a known redshift. Radio luminosity of FXT 210423 at $z \geqslant 1$ is consistent with that of the population of SGRB radio afterglows.

treat these measurements as upper limits on the optical brightness of a potential optical counterpart of FXT 210423. We use the E. L. Fitzpatrick (1999) extinction model with $A_v = 0.5422$ mag to correct for Milky Way reddening.

Additionally, we collected optical observations of FXT 210423 from the literature (I. Andreoni et al. 2021a, 2021b; A. Rossi et al. 2021; L. Xin et al. 2021; D. Eappachen et al. 2023), and we extracted photometry using the standard Zwicky Transient Facility (ZTF; E. C. Bellm et al. 2019; M. J. Graham et al. 2019) forced photometry service hosted by IPAC (F. J. Masci et al. 2023; see Table 4 in the Appendix).

3. Constraints on Relativistic Jets

3.1. Distance to the Source

Below we use a number of different arguments to try to infer boundaries on the distance of the FXT 210423. First, we used our Keck g-band detection of an extended source at the location of FXT 210423 to infer an upper limit on its distance based on the Lyman break. We found the limit to be $z < 4.16$, which is notably higher than the typical SGRB redshift of $z \lesssim 1$ (A. E. Nugent et al. 2022). S. Ai & B. Zhang (2021) associate the X-ray emission from FXT 210423 to the emission from a post-NS merger magnetar and infer an upper limit on the

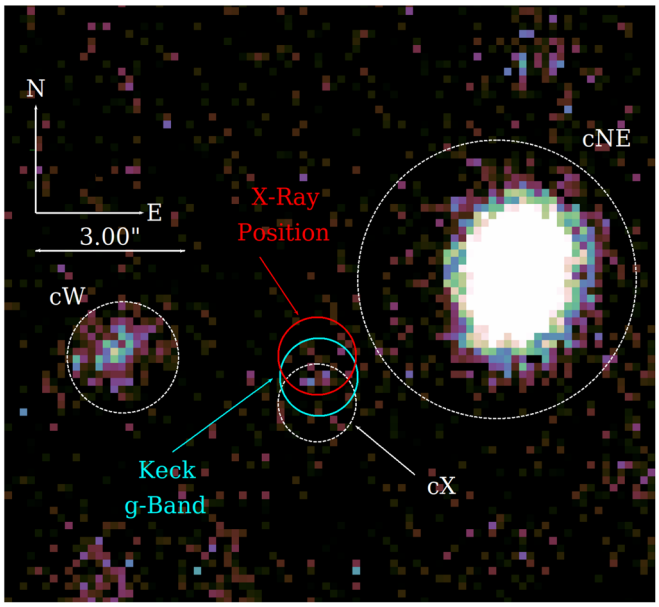

Figure 4. Keck g-band image of the field of FXT 210423 acquired on 2021 May 11 ($\delta t = 18.03$ days since discovery). Red region: $0\farcs7$ radius region at the location of the X-ray source from the CXO discovery images as determined with `wavdetect`. Cyan region: $0\farcs7$ radius region at the location of the extended source that we have identified in our Keck g-band images. We also mark the three extended sources ("cX," "cW," and "cNE") identified as potential host galaxies by D. Eappachen et al. (2023). Our Keck source is coincident with "cX" and we consider "cX" the most likely host galaxy for this FXT. North is up and east is right.

redshift of the source based on theoretical arguments related to the physical details of the origin of the X-ray emission (i.e., "free zone," "trapped zone," or "jet zone") and the fraction of magnetar spin-down luminosity dissipated as X-ray emission, η_x. For $\eta_x = 10^{-2}$, S. Ai & B. Zhang (2021) derived $z \leqslant 3.5$, which we adopt here as our high-redshift value. We adopt two intermediate-redshift values of $z = 1.51$ and $z = 1.04$ based on the known or photometric redshifts of potential host galaxies. Specifically, three potential host galaxies "cX," "cW," and "cNE" have been identified (Figure 4). "cNE" (i.e., SDSS J134856.75+263946.7) has a measured spectroscopic redshift of $z = 1.51$ (P. Jonker et al. 2021; D. Eappachen et al. 2023), while "cW" is found to have a photometric redshift of $z = 1.04$ (D. Eappachen et al. 2023). No redshift measurement is available for the most likely host, which is source "cX" (coincident with our extended Keck g-band source and the X-ray position of the FXT).

Finally, the lowest redshift value that we consider ($z = 0.063$) comes from the initially proposed association of the event with the galaxy cluster A1795 (D. Lin et al. 2021) at $d \approx 290$ Mpc. While the physical association with the A1795 cluster is likely to be due to chance alignment (D. Eappachen et al. 2023), we carry out simulations at this redshift to quantitatively demonstrate what constraints can be placed on the presence of relativistic jets in FXTs were an FXT to be found at these very close distances.

3.2. Jet-afterglow Light-curve Simulations with BOXFIT

FXTs have been associated in the literature with manifestations of NS mergers (e.g., F. E. Bauer et al. 2017), which are known to be capable of launching relativistic jets (e.g., E. Berger 2014; W.-f. Fong et al. 2015; A. Goldstein et al. 2017; E. Nakar 2020; R. Margutti & R. Chornock 2021). In order to constrain the parameter space of relativistic jets potentially associated with FXT 210423, we carried out a series of jet-afterglow emission simulations using the publicly available multiband light-curve generator `BOXFIT v2` (H. van Eerten et al. 2010), which is based on two-dimensional hydrodynamics simulations of relativistic jets with energy uniformly distributed within the jet opening angles (top-hat jets).

Table 3
Adopted Values of the Parameters for the `BOXFIT` Jet-afterglow Simulations

Parameter	Values Considered
z	0.063, 1.04, 1.51, 3.5
$\theta_{\rm obs}$ (deg)	0, 10, 20, 30, 40, 50, 60, 70, 80
θ_j (deg)	1, 2, 3, 4, 5, 6, 10, 15
$E_{\rm k,iso}$ (erg)	10^{48}, 10^{49}, 10^{50}, 10^{51}, 10^{52}, 10^{53}, 10^{54}, 10^{55}
ϵ_B	10^{-1}, 10^{-2}, 10^{-3}, 10^{-4}
n (cm^{-3})	10^{-1}, 10^{-2}, 10^{-3}, 10^{-4}, 10^{-5}, 10^{-6}

Note. All simulations assume $\epsilon_e = 0.1$ and $p = 2.4$.

The jet-afterglow emission detectable after an NS merger is thought to originate from the synchrotron emission of relativistic electrons accelerated at the shock front (T. Piran 2004). The evolution of the synchrotron radiation can reveal details about the geometry of the jet (i.e., the jet opening angle θ_j), the observer's angle relative to the jet axis ($\theta_{\rm obs}$), the kinetic energy of the outflow (E_k), the density of the surrounding medium (n), the fraction of the postshock energy transferred into magnetic fields (ϵ_B) and relativistic electrons (ϵ_e), and the distribution of energy in the relativistic electrons that produce synchrotron emission (here parameterized as a power law $N_e(\gamma_e) \propto \gamma_e^{-p}$, where γ_e is the electron Lorentz factor). Placing constraints on the true energy and the opening angles of these jets can provide insight into the launching mechanism of the relativistic outflow, while constraints on the density of the medium can provide insights into the progenitor model (M. Shibata & K. Hotokezaka 2019; A. Rouco Escorial et al. 2023). This is especially interesting for FXTs, as their origin is still debated.

We explored a wide range of parameter values (reported in Table 3) motivated by inferences derived from modeling of SGRB afterglows in the literature (e.g., W.-f. Fong et al. 2015; A. Rouco Escorial et al. 2023). For all simulations, we fixed the value of fractional postshock energy in relativistic electrons $\epsilon_e = 0.1$ (L. Sironi et al. 2015). The power-law index of the electron distribution was fixed to a value consistent with the median value from W.-f. Fong et al. (2015) of a sample of 38 SGRBs, $p = 2.4$. The beaming-corrected jet kinetic energy (i.e., the true energy) $E_{\rm k}$ is related to the isotropic equivalent energy as $E_{\rm k} = E_{\rm k,iso}(1 - \cos\theta_{\rm j})$, (e.g., D. A. Frail et al. 2001). Finally, we ran simulations of the radio, optical, and X-ray emission from relativistic jets at four different redshift values to reflect a variety of proposed distances to the source (i.e., $z = 3.5$, $z = 1.51$, $z = 1.04$, and $z = 0.063$), which we discuss in detail in Section 3.1.

For each combination of the parameters above we simulated the resulting synchrotron emission between 10 and 1000 days for observed frequencies $\nu_{\rm obs} = 0.65$, 6, 10, and 15 GHz (radio) and at 10 optical frequencies between $\nu_{\rm obs} = (3.143 \text{ and } 6.369) \times 10^{14}$ Hz. For the X-rays, we used 1 keV as the central frequency. For the

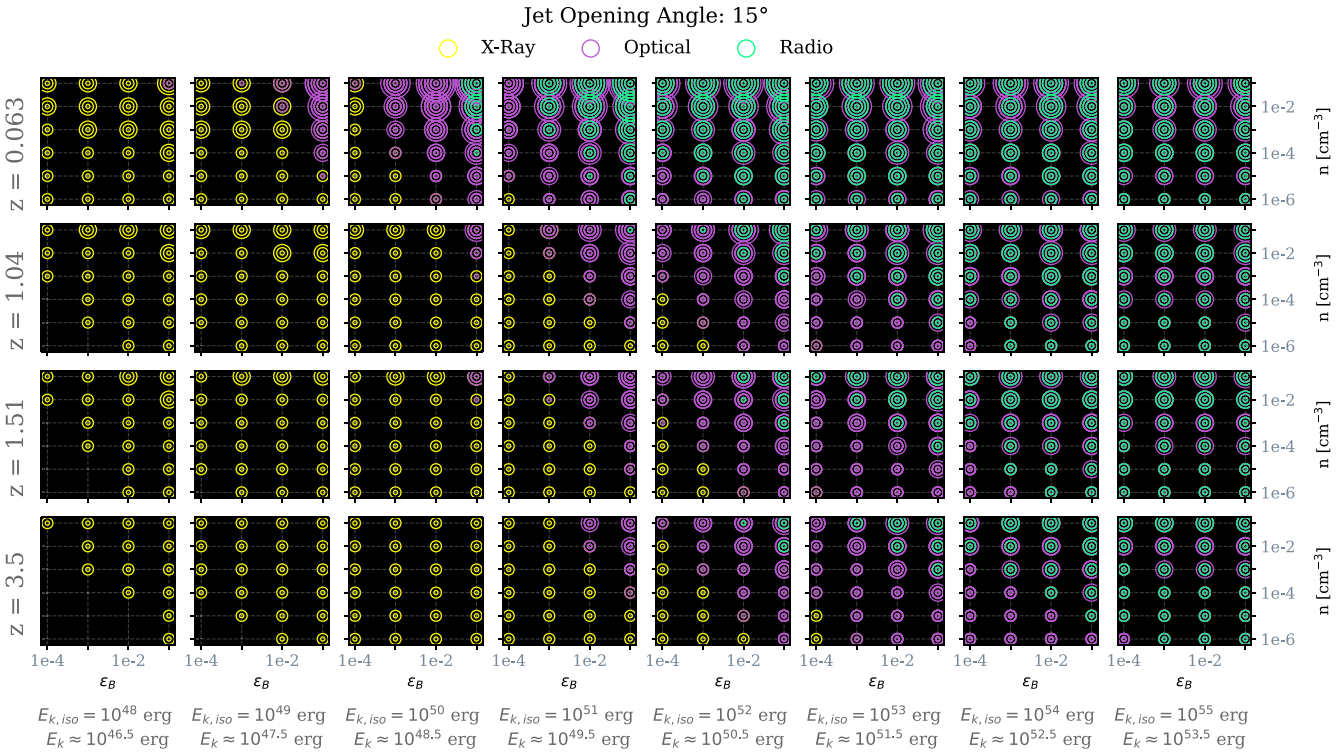

Figure 5. Grid representation of simulations that violate observations for a jet with $\theta_j = 15°$. Violations occur when either the radio, optical, or X-ray value of an observation exceeds that of the simulation at the corresponding observation time. Colored rings indicate a violation in a particular band (green: radio; purple: optical; and yellow: X-ray). The size of the ring indicates the observation angle of the simulation where the violation occurred with the innermost ring representing a violation of 0° and each proceeding concentric ring representing an increase of 10°. A set of nine concentric rings, in any color, consequently indicates that any jet with these properties are ruled out. Columns and rows of the outer grid indicate the energy and distance of the simulation. Columns and rows of each inner box indicate the fraction of the postshock energy transferred into magnetic fields (ϵ_B) and the density of the surrounding medium (n) in the simulation. The violation results are overlaid in the order radio (top), optical (middle), and X-ray (last), meaning the appearance of a radio or optical violation may cover an X-ray violation. The ordering has been chosen to best represent the overall shape of the violations. Any crossing on the grid with no ring indicates no constraints could be placed on simulations with the given parameters.

X-rays and optical, we ran simulations starting from the deceleration timescale (≈few hundred seconds) until 1000 days. Each simulated light curve is compared with our radio and optical nondetections of the afterglow. We consider the detected X-ray emission as an upper limit on the X-ray brightness of a jet afterglow at that time. A given parameter set is deemed viable if it does not violate any observational constraint. Our results are shown in Figures 5 and 6 and discussed in Section 4.

4. Discussion and Future Prospects

We discuss in this section what part of the parameter space of relativistic jets is ruled out by the multiwavelength observations of FXT 210423 in the broader context of SGRB-like jets through discussion of a wide jet ($\theta_j = 15°$) and a narrow jet ($\theta_j = 3°$). We end this section with a look at future observational campaigns of new FXTs that are now regularly announced by missions like the EP (W. Yuan et al. 2022).

For our wider jet $\theta_j = 15°$ case, Figure 5 shows that the entire region of the parameter space is allowed for very off-axis angles $\theta_{\rm obs} > 70°$, which is a consequence of the fainter emission from such jets that are not probed by our observations. Instead, for the roughly on-axis case (i.e., $\theta_{\rm obs} \leqslant 10°$), we can rule out all combinations of parameters aside from the low-energy, low-density cases (i.e., $E_{k,\rm iso} = 10^{48}$–10^{49} erg, $n = 10^{-4}$–10^{-2} cm^{-3}) in the lower left of the grid. We note that at intermediate off-axis angles $10° \leqslant \theta_{\rm obs} \leqslant 50°$ we are most sensitive (i.e., our observations rule out a larger portion of the parameter space) for jets with $E_{k,\rm iso} = 10^{50}$–10^{52} erg, which is a consequence of the fact that for these jets, the time of the observed peak of the emission is better coupled with the time when the observations had been acquired. Finally, we comment on the region of parameter space that is typical of cosmological SGRBs, LGRBs, and TDEs, using the results from W.-f. Fong et al. (2015), T. Laskar et al. (2015), K. D. Alexander et al. (2020), and T. Eftekhari et al. (2018). For typical SGRB energies $E_{k,\rm iso} = 10^{50}$–10^{53} erg inferred assuming $\epsilon_B = 0.1$, and typical low-density media with $n = 10^{-3}$ cm^{-3} (W.-f. Fong et al. 2015), Figure 5 shows that we can rule out all combinations of parameters for jets viewed at a $\theta_{\rm obs} \leqslant 10°$. We conclude that FXT 210423 did not harbor a wide SGRB-like jet with $\theta_j = 15°$ viewed at $\theta_{\rm obs} \leqslant 10°$ even for the largest redshift $z = 3.5$ considered in our simulations.

For the same range of $E_{k,\rm iso}$ values, off-axis collimated jets will produce intrinsically fainter emission (because of the lower E_k), making the detection of such systems more challenging. This is clearly demonstrated by Figure 6, where we present the results for a jet with $\theta_j = 3°$. Although we see similar trends to the wider-jet angle case, with more parameter space ruled out at higher energies, higher densities, larger ϵ_B values, and lower distances to the source, for highly collimated jets with $\theta_j = 3°$, we can only rule out on-axis systems for the majority of the parameter space, the exception being the low-energy, low-density cases ($E_{k,\rm iso} \leqslant 10^{49}$ erg and $n \leqslant 10^{-2}$) in the lower left of the grid.

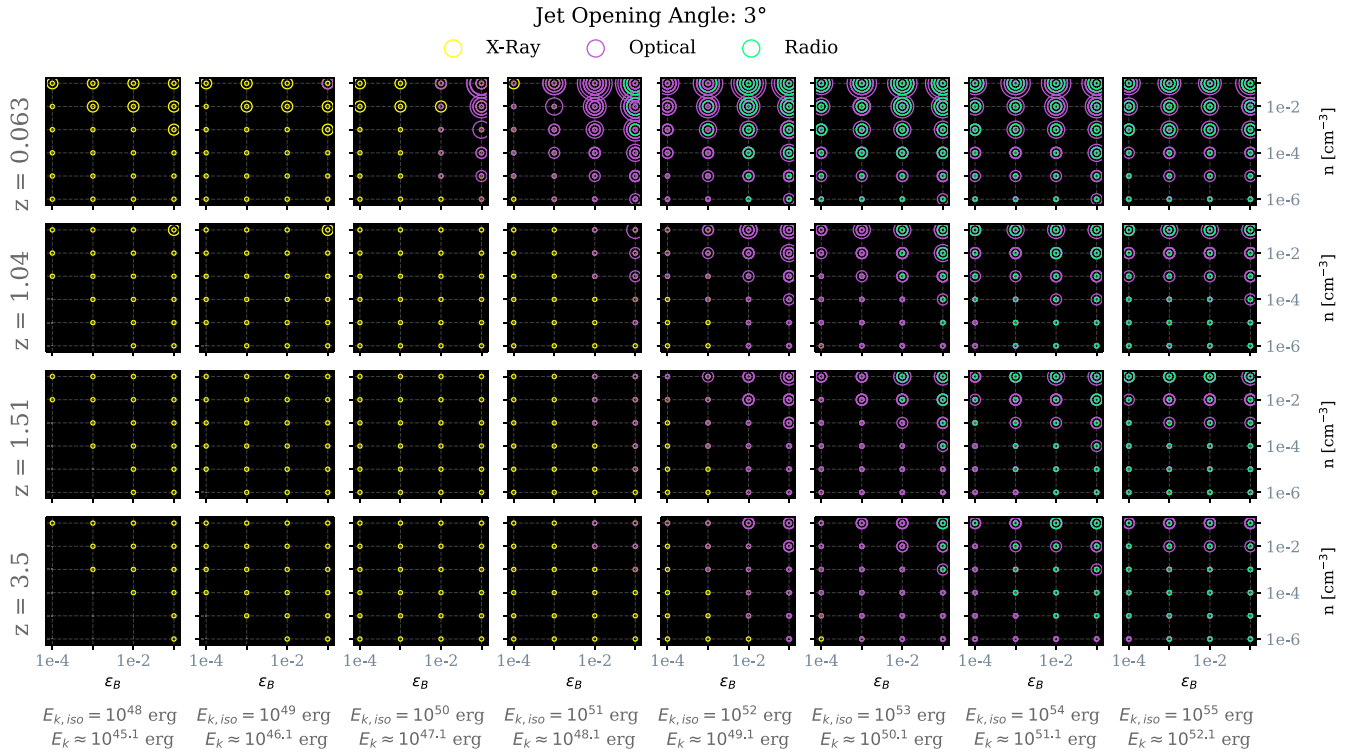

Figure 6. Same representation as Figure 5 for a jet with $\theta_j = 3°$.

LGRBs span a wide range of kinetic energies and densities. We focus our discussion on a representative range of values of $E_{k,\rm iso} = 10^{50}$–10^{52} erg and $n = 10^{-2}$–10^{2} cm^{-3} (inferred for $\epsilon_B = 0.1$; see, e.g., T. Laskar et al. 2015). With reference to Figure 5, we find that we can rule out all combinations of parameters of jets viewed at a $\theta_{\rm obs} \leqslant 10°$, bringing us to the conclusion that FXT 210423 had no LGRB-like jet with $\theta_j = 15°$ viewed at $\theta_{\rm obs} \leqslant 10°$.

The inferred kinetic energy of prompt on-axis TDE jets from supermassive BHs tends to cover the upper end of the energy range that we have investigated ($E_{k,\rm iso} \geqslant 10^{52}$ erg s^{-1}; e.g., T. Eftekhari et al. 2018), with densities $n \geqslant 0.1$ cm^{-3}.[21] For this combination of parameters, and assuming equipartition, we can rule out jets viewed at a $\theta_{\rm obs} \leqslant 20°$, bringing us to the conclusion that FXT 210423 had no TDE jet with $\theta_j = 15°$ viewed at $\theta_{\rm obs} \leqslant 20°$.

We conclude with considerations on future observations of newly discovered FXTs. Our radio observations of the FXT 210423 demonstrated the constraining power of prompt radio observations of these systems in the first few weeks after discovery. It is clear that rapid radio follow-up of future FXTs immediately after discovery can place valuable constraints on the presence and properties of on-axis jets (if there). However, from our results, it is also equally clear that for intrinsically low-energy jets (e.g., highly collimated jets) viewed off-axis, very deep, late-time follow-up observations on timescales of months to years are necessary. Sub-μJy observations from the Square Kilometre Array and next-generation VLA could be particularly constraining. The combination of prompt and late-time deep radio observations of the most nearby FXTs discovered by the EP will constrain the presence of relativistic jets in these systems and will illuminate their connection (or lack thereof) to NS mergers.

[21] We acknowledge that our assumed interstellar medium-like density profile might not be representative of density profiles inferred for SMBH TDEs, see, e.g., K. D. Alexander et al. (2020), their Figure 2, and that IMBH TDEs might have different energetics than SMBH TDEs.

Acknowledgments

The National Radio Astronomy Observatory is a facility of the National Science Foundation operated under cooperative agreement by Associated Universities, Inc. The Keck observations presented in this paper were enabled by access provided by Northwestern University and CIERA. The ZTF forced-photometry service was funded under the Heising-Simons Foundation grant #12540303 (PI: M. Graham). This research used the Savio computational cluster resource provided by the Berkeley Research Computing program at the University of California, Berkeley (supported by the UC Berkeley Chancellor, Vice Chancellor for Research, and Chief Information Officer). R.M. acknowledges support by the National Science Foundation under award No. AST-2221789 and AST-2224255. The TReX team at UC Berkeley is partially funded by the Heising-Simons Foundation under grant 2021-3248 (PI: R. Margutti). D.L. acknowledges support by the National Aeronautics and Space Administration through Chandra Award No. DD1-22128X issued by the Chandra X-ray Observatory Center and through the ADAP grant No. 80NSSC22K0218. This paper employs a list of Chandra data sets, obtained by the Chandra X-ray Observatory, contained in doi:10.25574/cdc.300.

Facilities: VLA, CXO, Keck:I.

Software: BOXFIT, GNU.

Appendix
Optical Data

Table 4 shows optical observations of the field of FXT 210423 in the days following the detection of the transient along with inferred brightness at the location of the transient.

Table 4
Optical Observations of the Field of FXT 210423 and Inferred Brightness at the Location of the Transient

Facility Observatory	Observation (MJD)	Days Since T_0 (days)	Filter	Magnitude (AB)	Extinction-corrected Magnitude (AB)	Reference
Keck	59345.96	18.03	*g*	>25.8	>25.14	This work
Keck	59345.96	18.03	*i*	>25.4	>24.97	This work
ZTF	59335.37	7.44	*i*	>19.6	>19.3	(1)
ZTF	59338.34	10.41	*i*	>20.4	>20.1	This work
ZTF	59341.26	13.33	*i*	>20.9	>20.6	This work
ZTF	59344.35	16.42	*i*	>20.5	>20.2	This work
ZTF	59352.37	24.44	*i*	>20.3	>20.0	This work
ZTF	59353.25	25.32	*i*	>20.2	>19.9	This work
ZTF	59355.32	27.29	*i*	>18.9	>18.6	This work
ZTF	59359.34	31.41	*i*	>19.8	>19.5	This work
ZTF	59362.34	34.41	*i*	>20.5	>20.2	This work
ZTF	59365.37	37.44	*i*	>19.9	>19.6	This work
ZTF	59328.27	0.34	*r*	>20.9	>20.5	(1)
ZTF	59329.33	1.40	*r*	>20.7	>20.3	This work
ZTF	59334.32	6.39	*r*	>21.4	>21.0	This work
ZTF	59335.29	7.36	*r*	>20.8	>20.4	This work
ZTF	59336.34	8.41	*r*	>21.6	>21.2	This work
ZTF	59338.28	10.35	*r*	>21.5	>21.1	This work
ZTF	59339.27	11.34	*r*	>21.3	>20.9	This work
ZTF	59340.31	12.38	*r*	>21.7	>21.3	This work
ZTF	59341.23	13.30	*r*	>21.5	>21.1	This work
ZTF	59342.35	14.42	*r*	>21.6	>21.2	This work
ZTF	59343.22	15.29	*r*	>21.6	>21.2	This work
ZTF	59344.34	16.41	*r*	>21.7	>21.3	This work
ZTF	59345.26	17.33	*r*	>21.4	>21.0	This work
ZTF	59346.39	18.46	*r*	>21.7	>21.3	This work
ZTF	59349.31	20.38	*r*	>22.1	>21.7	This work
ZTF	59349.28	21.35	*r*	>21.6	>21.2	This work
ZTF	59350.27	22.34	*r*	>21.6	>21.2	This work
ZTF	59352.25	24.32	*r*	>21.3	>20.9	This work
ZTF	59353.30	25.37	*r*	>21.0	>20.6	This work
ZTF	59354.24	26.31	*r*	>21.1	>20.7	This work
ZTF	59355.23	27.30	*r*	>20.3	>19.9	This work
ZTF	59356.28	28.35	*r*	>20.8	>20.4	This work
ZTF	59358.32	30.39	*r*	>20.3	>19.9	This work
ZTF	59359.22	31.29	*r*	>20.6	>20.2	This work
ZTF	59361.35	33.42	*r*	>20.8	>20.4	This work
ZTF	59362.25	34.32	*r*	>21.3	>20.9	This work
ZTF	59363.34	35.41	*r*	>21.2	>20.8	This work
ZTF	59364.30	36.37	*r*	>21.6	>21.2	This work
ZTF	59328.34	0.41	*g*	>20.5	>19.8	(1)
ZTF	59329.27	1.34	*g*	>20.1	>19.4	This work
ZTF	59331.47	3.54	*g*	>19.4	>18.7	This work
ZTF	59334.22	6.29	*g*	>22.0	>21.3	This work
ZTF	59335.29	7.36	*g*	>21.3	>20.6	This work
ZTF	59336.34	8.41	*g*	>21.3	>20.6	This work
ZTF	59338.36	10.43	*g*	>21.8	>21.1	This work
ZTF	59339.23	11.3	*g*	>21.6	>20.9	This work
ZTF	59340.36	12.43	*g*	>21.6	>20.9	This work
ZTF	59341.3	13.37	*g*	>21.8	>21.1	This work
ZTF	59342.34	14.41	*g*	>21.2	>20.5	This work
ZTF	59343.27	15.34	*g*	>21.7	>21.0	This work
ZTF	59344.31	16.38	*g*	>22.2	>21.5	This work
ZTF	59345.20	17.27	*g*	>21.8	>21.1	This work
ZTF	59346.35	18.42	*g*	>21.8	>21.1	This work
ZTF	59348.34	20.41	*g*	>22.2	>21.5	This work
ZTF	59352.20	24.27	*g*	>21.0	>20.3	This work
ZTF	59353.34	25.41	*g*	>21.1	>20.4	This work
ZTF	59354.33	26.40	*g*	>21.0	>20.3	This work
ZTF	59355.30	27.37	*g*	>20.3	>19.6	This work
ZTF	59356.22	28.29	*g*	>20.7	>20.0	This work
ZTF	59358.40	30.47	*g*	>20.1	>19.4	This work
ZTF	59359.27	31.34	*g*	>20.3	>19.6	This work

Table 4
(Continued)

Facility Observatory	Observation (MJD)	Days Since T_0 (days)	Filter	Magnitude (AB)	Extinction-corrected Magnitude (AB)	Reference
ZTF	59361.29	33.36	g	>20.8	>20.1	This work
ZTF	59362.21	34.28	g	>21.0	>20.3	This work
ZTF	59363.26	35.33	g	>21.3	>20.6	This work
ZTF	59364.29	36.36	g	>21.1	>20.4	This work
ZTF	59365.29	37.36	g	>21.1	>20.4	This work
LBT	59342.31	14.38	z	>25.1	>24.88	(3)
LBT	59342.31	14.38	r	>26.1	>25.66	(3)
Xinglong	59339.53	11.60	I	>20.5	>20.2	(2)
Palomar WaSP	59340.30	12.37	i	>24.8	>24.32	(4)
Palomar WaSP	59340.30	12.37	r	>25.2	>24.76	(4)
VLT	59340	13	R	>24.7	>24.29	(5)
GTC	59375	47	u	>26.2	>25.35	(5)
GTC	59375	47	g	>27.0	>26.56	(5)
GTC	59375	47	r	>26.1	>25.66	(5)
GTC	59375	47	i	>24.4	>24.08	(5)
GTC	59375	47	z	>24.7	>24.46	(5)

References. (1) I. Andreoni et al. (2021b); (2) L. Xin et al. (2021); (3) A. Rossi et al. (2021); (4) I. Andreoni et al. (2021a); (5) D. Eappachen et al. (2023).
(This table is available in machine-readable form in the online article.)

ORCID iDs

Dina Ibrahimzade https://orcid.org/0009-0008-0782-5028
R. Margutti https://orcid.org/0000-0003-4768-7586
J. S. Bright https://orcid.org/0000-0002-7735-5796
P. Blanchard https://orcid.org/0000-0003-0526-2248
K. Paterson https://orcid.org/0000-0001-8340-3486
D. Lin https://orcid.org/0000-0001-5683-5339
H. Sears https://orcid.org/0000-0001-8023-4912
A. Polzin https://orcid.org/0000-0002-5283-933X
I. Andreoni https://orcid.org/0000-0002-8977-1498
G. Schroeder https://orcid.org/0000-0001-9915-8147
K. D. Alexander https://orcid.org/0000-0002-8297-2473
E. Berger https://orcid.org/0000-0002-9392-9681
D. L. Coppejans https://orcid.org/0000-0001-5126-6237
A. Hajela https://orcid.org/0000-0003-2349-101X
J. Irwin https://orcid.org/0000-0003-4307-8521
T. Laskar https://orcid.org/0000-0003-1792-2338
B. D. Metzger https://orcid.org/0000-0002-4670-7509
J. C. Rastinejad https://orcid.org/0000-0002-9267-6213
L. Rhodes https://orcid.org/0000-0003-2705-4941

References

Ai, S., & Zhang, B. 2021, ApJL, 915, L11
Alexander, K. D., van Velzen, S., Horesh, A., & Zauderer, B. A. 2020, SSRv, 216, 81
Alp, D., & Larsson, J. 2020, ApJ, 896, 39
Andreoni, I., Coughlin, M. & Zwicky Transient Facility 2022a, AAS Meeting, 240, 307.05
Andreoni, I., Coughlin, M. W., Perley, D. A., et al. 2022b, Natur, 612, 430
Andreoni, I., De, K., Kasliwal, M., & Tzanidakis, A. 2021a, ATel, 14640, 1
Andreoni, I., Kasliwal, M., & Graham, M. 2021b, ATel, 14600, 1
Bauer, F. E., Treister, E., Schawinski, K., et al. 2017, MNRAS, 467, 4841
Bellm, E. C., Kulkarni, S. R., Graham, M. J., et al. 2019, PASP, 131, 018002
Berger, E. 2014, ARA&A, 52, 43
Berger, E., Price, P. A., Cenko, S. B., et al. 2005, Natur, 438, 988
Bloom, J. S., Giannios, D., Metzger, B. D., et al. 2011, Sci, 333, 203
Briggs, D. S. 1995, PhD thesis, New Mexico Inst. Mining and Technology
Bright, J., Carotenuto, F., Jonker, P. G., Fender, R., & Smartt, S. 2024, GCN, 36362, 1
Brown, G. C., Levan, A. J., Stanway, E. R., et al. 2015, MNRAS, 452, 4297
Bruni, G., Rhodes, L., Piro, L., et al. 2024, GCN, 35980, 1
Burrows, D. N., Kennea, J. A., Ghisellini, G., et al. 2011, Natur, 476, 421
Carotenuto, F., Bright, J., Jonker, P. G., Fender, R., & Rhodes, L. 2024, GCN, 35961, 1
Cenko, S. B., Krimm, H. A., Horesh, A., et al. 2012, ApJ, 753, 77
Clarke, T. E., Kassim, N. E., Brisken, W., et al. 2016, Proc. SPIE, 9906, 99065B
De Luca, A., Stelzer, B., Burgasser, A. J., et al. 2020, A&A, 634, L13
De Luca, A., Tiengo, A., D'Agostino, D., et al. 2016, in XMM-Newton: The Next Decade, ed. J. U. Ness (Paris: ESA), 42
Eappachen, D., Jonker, P., Levan, A., et al. 2023, ApJ, 948, 91
Eappachen, D., Jonker, P. G., Quirola-Vásquez, J., et al. 2024, MNRAS, 527, 11823
Eftekhari, T., Berger, E., Zauderer, B. A., Margutti, R., & Alexander, K. D. 2018, ApJ, 854, 86
Fernández, R., Margalit, B., & Metzger, B. D. 2019, MNRAS, 488, 259
Fitzpatrick, E. L. 1999, PASP, 111, 63
Fong, W., Laskar, T., Rastinejad, J., et al. 2021, ApJ, 906, 127
Fong, W.-f., Berger, E., Margutti, R., & Zauderer, B. A. 2015, ApJ, 815, 102
Fong, W.-f., Berger, E., Metzger, B. D., et al. 2013, ApJ, 780, 118
Fong, W.-f., Nugent, A. E., Dong, Y., et al. 2022, ApJ, 940, 56
Frail, D. A., Kulkarni, S. R., Sari, R., et al. 2001, ApJ, 562, L55
Fruscione, A., McDowell, J. C., Allen, G. E., et al. 2006, Proc. SPIE, 6270, 62701V
Gillanders, J., Rhodes, L., Srivastav, S., et al. 2024, ApJ, 969, 14
Glennie, A., Jonker, P. G., Fender, R. P., Nagayama, T., & Pretorius, M. L. 2015, MNRAS, 450, 3765
Goldstein, A., Veres, P., Burns, E., et al. 2017, ApJL, 848, L14
Graham, M. J., Kulkarni, S. R., Bellm, E. C., et al. 2019, PASP, 131, 078001
Hajela, A., Margutti, R., Bright, J. S., et al. 2022, ApJL, 927, L17
HI4PI Collaboration, Ben Bekhti, N., Flöer, L., et al. 2016, A&A, 594, A116
Ho, A. Y. Q. 2020, ATel, 13485, 1
Irwin, J. A., Maksym, W. P., Sivakoff, G. R., et al. 2016, Natur, 538, 356
Jonker, P. 2023, EP240414A, an Einstein Probe fast X-ray transient bridging Luminous Fast Blue Optical Transients and Long Gam, Chandra Proposal ID #25208994, The Chandra X-Ray Center
Jonker, P., Levan, A., Torres, M., Eappachen, D., & Quirola, J. 2021, TNSAN, 160, 1
Jonker, P. G., Glennie, A., Heida, M., et al. 2013, ApJ, 779, 14
Knust, F., Greiner, J., Van Eerten, H., et al. 2017, A&A, 607, A84
Laskar, T., Berger, E., Margutti, R., et al. 2015, ApJ, 814, 1
Laskar, T., Escorial, A. R., Schroeder, G., et al. 2022, ApJL, 935, L11
Leung, J. K., Ricci, R., Dobie, D., & Troja, E. 2024, GCN, 35968, 1
Levan, A. J., Jonker, P. G., Saccardi, A., et al. 2024, arXiv:2404.16350
Levan, A. J., Tanvir, N. R., Cenko, S. B., et al. 2011, Sci, 333, 199
Lin, D., Irwin, J. A., & Berger, E. 2021, ATel, 14599, 1
Lin, D., Irwin, J. A., Berger, E., & Nguyen, R. 2022, ApJ, 927, 211
Liu, Y., Sun, H., Xu, D., et al. 2024, arXiv:2404.16425

MacLeod, M., Guillochon, J., Ramirez-Ruiz, E., Kasen, D., & Rosswog, S. 2016, ApJ, 819, 3
Maguire, K., Eracleous, M., Jonker, P. G., MacLeod, M., & Rosswog, S. 2020, SSRv, 216, 39
Margutti, R., & Chornock, R. 2021, ARA&A, 59, 155
Masci, F. J., Laher, R. R., Rusholme, B., et al. 2023, arXiv:2305.16279
Mazzali, P. A., Valenti, S., Della Valle, M., et al. 2008, Sci, 321, 1185
McMullin, J. P., Waters, B., Schiebel, D., Young, W., & Golap, K. 2007, in ASP Conf. Ser. 376, Astronomical Data Analysis Software and Systems XVI, ed. R. A. Shaw, F. Hill, & D. J. Bell (San Francisco, CA: ASP), 127
Modjaz, M., Li, W., Butler, N., et al. 2009, ApJ, 702, 226
Nakar, E. 2020, PhR, 886, 1
Novara, G., Esposito, P., Tiengo, A., et al. 2020, ApJ, 898, 37
Nugent, A. E., Fong, W.-F., Dong, Y., et al. 2022, ApJ, 940, 57
Pasham, D. R., Cenko, S. B., Levan, A. J., et al. 2015, ApJ, 805, 68
Peng, Z.-K., Yang, Y.-S., Shen, R.-F., et al. 2019, ApJL, 884, L34
Piran, T. 2004, RvMP, 76, 1143
Polzin, A., Margutti, R., Coppejans, D. L., et al. 2023, ApJ, 959, 75
Quirola-Vásquez, J., Bauer, F., Jonker, P., et al. 2022, A&A, 663, A168
Quirola-Vásquez, J., Bauer, F. E., Jonker, P. G., et al. 2023, A&A, 675, A44
Rhodes, L., Bright, J. S., Fender, R., et al. 2023, MNRAS, 521, 389
Rossi, A., Cappellaro, E., & D'Avanz, P. 2021, ATel, 14635, 1
Rouco Escorial, A., Fong, W.-f., Berger, E., et al. 2023, ApJ, 959, 13
Saccardi, A., Levan, A. J., Zhu, Z., et al. 2024, GCN, 35936, 1
Sarin, N., Ashton, G., Lasky, P. D., et al. 2021, arXiv:2105.10108
Semena, A., Mereminskiy, I., Lutovinov, A., Molkov, S., & Pavlinsky, M. 2020, ATel, 13415, 1
Shibata, M., & Hotokezaka, K. 2019, ARNPS, 69, 41
Sironi, L., Keshet, U., & Lemoine, M. 2015, SSRv, 191, 519
Soderberg, A. M., Berger, E., Kasliwal, M., et al. 2006, ApJ, 650, 261
Soderberg, A. M., Berger, E., Page, K. L., et al. 2008, Natur, 453, 469
Somalwar, J. J., Ravi, V., Dong, D. Z., et al. 2023, ApJ, 945, 142
Srivastav, S., Smartt, S. J., Fulton, M. D., et al. 2024, GCN, 35932, 1
Sun, H., Li, Y., Zhang, B.-B., et al. 2019, ApJ, 886, 129
Surnis, M., Joshi, B. C., Maan, Y., et al. 2021, ATel, 14735, 1
van Eerten, H., Zhang, W., & MacFadyen, A. 2010, ApJ, 722, 235
Volnova, A., Kusakin, A., Moskvitin, A. S., et al. 2017, GCN, 21419, 1
Waxman, E., & Katz, B. 2017, Shock Breakout Theory (Berlin: Springer), 967
Wilms, J., Kreykenbohm, I., Weber, P., et al. 2020, ATel, 13416, 1
Xin, L., Wang, J., & Wei, J. 2021, ATel, 14610, 1
Xue, Y. Q., Zheng, X. C., Li, Y., et al. 2019, Natur, 568, 198
Yuan, Q., Wang, Q. D., Lei, W.-H., Gao, H., & Zhang, B. 2016, MNRAS, 461, 3375
Yuan, W., Zhang, C., Chen, Y., & Ling, Z. 2022, Handbook of X-ray and Gamma-ray Astrophysics (Berlin: Springer), 1
Zauderer, B. A., Berger, E., Soderberg, A. M., et al. 2011, Natur, 476, 425
Zhang, W. J., Mao, X., Zhang, W. D., et al. 2024, GCN, 35931, 1